INTERNATIONAL JOURNAL OF HYDROGEN ENERGY 42 (2017) 10131–10141

Available online at www.sciencedirect.com

ScienceDirect

journal homepage: www.elsevier.com/locate/he

Characteristics of A_2B_7-type La–Y–Ni-based hydrogen storage alloys modified by partially substituting Ni with Mn

Wei Xiong [a,b], Huizhong Yan [a,b,*], Li Wang [a,b], V. Verbetsky [c], Xin Zhao [a,b], S. Mitrokhin [c], Baoquan Li [a,b], Jin Li [a,b], Yan Wang [a,b]

[a] National Engineering Research Center of Rare Earth Metallurgy and Functional Materials, Baotou 014030, PR China
[b] Baotou Research Institute of Rare Earths, Baotou 014030, PR China
[c] Chemistry Department, Lomonosov Moscow State University, Leninskie Gory 1, Bldg. 3, Moscow 119991, Russian Federation

ARTICLE INFO

Article history:
Received 3 December 2016
Received in revised form
29 December 2016
Accepted 15 January 2017
Available online 7 February 2017

Keywords:
Hydrogen storage materials
La–Y–Ni alloy
Solid–H_2 reaction
Electrochemical properties
MH–Ni battery

ABSTRACT

$LaY_2Ni_{10.5-x}Mn_x$ ($x = 0.0, 0.5, 1.0, 2.0$) alloys are prepared by a vacuum induction-quenching process followed by annealing. The structure, as well as the hydriding/dehydriding and charging/discharging characteristics, of the alloys are investigated via X-ray diffraction (XRD), scanning electron microscopy with energy-dispersive X-ray spectroscopy (SEM-EDS), pressure-composition isotherms (PCI), and electrochemical measurement. The alloys have multiphase structures mainly composed of Gd_2Co_7-type (3R) and Ce_2Ni_7-type (2H) phases. Partial substitution of Ni by Mn clearly increases the hydrogen storage capacity of the alloys. The $x = 0.5$ alloy exhibits a maximum hydrogen storage capacity of 1.40 wt % and a discharge capacity of 392.9 mAh g^{-1}, which are approximately 1.5 and 1.9 times greater than those of the $x = 0.0$ alloy, respectively. The high-rate dischargeability (HRD) of the $x = 0.5$ alloy is higher than that of the other alloys because of its large hydrogen diffusion coefficient D, which is a controlling factor in the electrochemical kinetic performance of alloy electrodes at high discharge current densities. Although the cyclic stability of the $x = 0.5$ alloy is not as high as that of the other alloys, its capacity retention ratio is as high as 56.3% after the 400th cycle. The thermodynamic characteristics of the $x = 0.5$ alloy satisfy the requirements of the hydride electrode of metal hydride–nickel (MH–Ni) batteries.

© 2017 Hydrogen Energy Publications LLC. Published by Elsevier Ltd. All rights reserved.

Introduction

Intermetallic compounds RMn (R = rare earth; M = transition metal; $1 \leq n \leq 5$) can reversibly store a large amount of hydrogen and are therefore important energy storage materials [1–3]. According to the La–Ni binary phase diagram [4], phases such as RNi_3 and R_2Ni_7 may form during heating through peritectic reactions. Among the RNi_3-type compounds (R = La, Ce, Pr, Nd, Sm, Gd, Tb, Dy, Ho, Er, Y), YNi_3 exhibits the largest cell volume, lowest density, and most satisfactory electrochemical characteristics [5].

* *Corresponding author*. Baotou Research Institute of Rare Earths, Baotou 014030, PR China.
E-mail address: yhzmail@126.com (H. Yan).
http://dx.doi.org/10.1016/j.ijhydene.2017.01.080
0360-3199/© 2017 Hydrogen Energy Publications LLC. Published by Elsevier Ltd. All rights reserved.

The partial substitution of Y in YNi_3 compounds with La and/or Ce leads to the formation of ternary yttrium-based alloys having the general formula $La_{1-x}Ce_xY_2Ni_9$ ($0 \leq x \leq 1$) [1,6–8]. Similar to the R–Mg–Ni system superlattice alloys [9], these R–Y–Ni compounds adopt a rhombohedral structure of the $PuNi_3$ type, which can be described as an intergrowth between RNi_5- and RNi_2-type structures and induces greater receptivity to hydrogen than commercial RNi_5-type alloys. Furthermore, the Y element and Mg element have similar effects in the two series of hydrogen storage alloys. Both Mg in the La–Mg–Ni alloy and Y in the La–Y–Ni alloy increase the structural stability of the corresponding alloys in the hydrogenation/dehydrogenization process and avoid or delay the hydrogen-induced amorphous (HIA) of the alloys [10–12]. The lanthanum compound LaY_2Ni_9 absorbs 12.3 H/f.u. (formula unit), which corresponds to 380 mAh g^{-1} in equivalent electrochemical units under 1 bar of hydrogen gas, and its plateau pressure for absorption is 0.06 bar at 298 K [1]. Owing to these characteristics, ternary yttrium-based alloys are among the most promising negative electrode materials for metal hydride–nickel (MH–Ni) batteries.

In recent years, R–Mg–Ni system hydrogen storage alloys have been investigated extensively, and their discharge capacities have been found to be as high as 414 mAh g^{-1} [13–26]. However, the relatively high volatility of Mg makes the preparation process difficult and expensive [14,18–21], thereby restricting the application of this family of alloys. In contrast, R–Y–Ni alloys can be easily prepared by induction melting, which is also preferable for R–Mg–Ni alloys. However, the discharge capacity of the AB_3-type La–Y–Ni alloy is only 260 mAh g^{-1} [6–8], which requires further enhancement. In our previous work [27–29], we found that the electrochemical properties of AB_3-, A_2B_7-, and A_5B_{19}-type R–Y–Ni system alloys can be improved significantly by adjusting the alloy composition using the method of element substitution. The partial substitution of Ni by metals such as Mn and Al can significantly increase the discharge capacity of the alloys and provide an optimal trade-off between high hydrogen capacity and good cyclic stability.

Mn is an indispensable element in conventional mischmetal-based AB_5-type alloys for maintaining cycle stability and high-rate dischargeability (HRD) [30]. Nevertheless, the substitution of the Ni in the mischmetal-based superlattice alloys by Mn decreases both the gaseous phase and electrochemical capacities due to a reduction in the abundance of the main A_2B_7 phase. It additionally adversely affects alloy properties such as the phase homogeneity, capacity, cycle stability, HRD, and surface reaction due to deterioration in the surface catalytic ability as the Mn content increases [30]. However, the R–Mg–Ni system superlattice alloy family (AB_3, A_2B_7, A_5B_{19}) tends to focus on La- and Nd-only alloys, for which the partial substitution of Mn for Ni can increase the lattice parameters and the cell volume, decrease the plateau equilibrium pressure, increase the discharge capacity and improve the electrochemical catalytic activity of the alloys [22–24]. In practice, there exists an optimum content of Mn for improving the hydrogen storage property and overall electrochemical properties of the alloys. Mn might be suitable for dual tuning of the thermodynamic and kinetic properties of the Mn-containing hydrogen storage alloys [31].

A study of the effect of the partial substitution of Ni by Mn on the structure and properties of the A_2B_7-type $LaY_2Ni_{10.5}$ superlattice alloy is therefore necessary and is presented in the present work.

Experimental

The alloys designed as A_2B_7-type $LaY_2Ni_{10.5-x}Mn_x$ ($x = 0.0, 0.5, 1.0, 2.0$) were prepared under a 0.05 MPa argon atmosphere in a vacuum induction-quenching furnace with a copper wheel rotating at a linear velocity of 4.33 m s^{-1}. The purities of the component metals were at least 99 wt %. An appropriate excess (2 wt % La, 2 wt % Y and 5 wt % Mn) of some component metals were added to compensate for evaporative loss. The chemical compositions of the alloys were examined by inductively coupled plasma (ICP) system and the results were in good agreement with the nominal compositions. The alloys were annealed in vacuum less than 10^{-2} Pa at 1148 K for 16 h, and the prepared alloy flakes were mechanically pulverized into powder particles, ranging from 38 μm to 74 μm in size, for electrochemical measurements.

The phases of the alloy powders were characterized by X-ray diffraction (XRD) using a Philips-PW 1700 X powder diffractometer with Cu Kα radiation at 40 kV and 200 mA and a scan rate of 0.02° min^{-1}, and the diffraction patterns were analyzed via Rietveld refinement (using a software program called Maud). The morphologies of the alloys were examined via scanning electron microscopy (SEM; HITACHI S-3400N) with energy-dispersive X-ray spectroscopy (EDS).

Pressure-composition isotherms (PCI) were obtained over the pressure range of 10^{-3} MPa to 2.0 MPa at temperatures of 298 K, 313 K, 328 K, and 343 K in a Sievert testing device. The alloy flakes were mechanically broken into small particles ranging from 74 μm to 1.2 mm in size before testing so that fresh alloy surfaces were exposed to hydrogen gas. Alloy samples having a mass of approximately 5 g were placed in the reaction chamber, which was evacuated for 60 min at the test temperature, and then allowed to react with hydrogen gas (99.999% purity) under a pressure of 2 MPa. The chamber was then slowly cooled to room temperature and maintained at that temperature for 30 min. Dehydriding was performed by heating the chamber to the test temperature and evacuating it for 60 min until the hydrogen pressure was less than 10^{-3} MPa. Three hydriding/dehydriding cycles were performed to ensure that the alloys were fully activated.

MH electrodes were prepared by mixing 0.1 g of alloy powder with 0.4 g of carbonyl nickel powder and then cold-pressing the mixture into pellets with a diameter of 15 mm under a pressure of 16 MPa. Each pellet was then placed between two Ni gauze layers, and the edges were tightly spot welded to maintain good electrochemical contact between the pellet and the Ni gauze. A Ni lead wire was then attached to the Ni gauze by spot welding to prepare the hydrogen storage alloy electrode (MH electrode). Electrochemical measurements were performed in a half-cell consisting of the prepared MH electrode and a sintered $Ni(OH)_2$/NiOOH counter electrode with excess capacity immersed in 6 mol L^{-1} KOH electrolyte. The discharge capacity and cyclic stability were measured using a galvanostatic method as follows: each prepared

electrode was charged at a 0.2 C rate for 6 h, followed by a 5-min break, and then, the electrode was discharged at a 0.2 C rate to the cut-off potential of 1.0 V versus the counter electrode. Linear polarization curves were obtained, and potential step measurements were carried out after the electrodes were activated on a CHI 660D electrochemical workstation. The linear polarization curves were obtained by scanning the electrode potential at a rate of 0.1 mV s^{-1} from −5 to 5 mV at a 50% depth of discharge (DOD). For the potential step measurement, the electrodes in the fully charged state were discharged at potential steps of +500 mV for 3600 s. The average particle radius of the alloys was measured using a Sympatec laser particle analyzer (HELOS H2358 and RODOS) and found to be approximately 22.35 × 10^{-4} cm. All the tests were conducted at room temperature (298 K).

Results and discussion

Phase structure

Fig. 1 shows the Rietveld refinement of the XRD profiles of the $LaY_2Ni_{10.5-x}Mn_x$ (x = 0.0, 0.5, 1.0, 2.0) alloys. The phase abundance, cell parameters, and internal strain are listed in Table 1. All the alloys have multiphase structures composed of Gd_2Co_7-type (3R) and Ce_2Ni_7-type (2H) phases; in addition, the x = 0.0 alloy contains a small amount of the Ce_5Co_{19}-type (3R) phase (2.04%) and a very small amount of the $PuNi_3$-type (3R) phase (1.38%). As the Mn content increases, the abundance of the Gd_2Co_7-type phase decreases from 51.84% (x = 0.0) to 23.03% (x = 2.0), whereas the abundance of the Ce_2Ni_7-type phase shows the opposite trend. Both the lattice parameters and the cell volume of the Gd_2Co_7- and Ce_2Ni_7-type phases increase with increasing manganese content, which is mainly ascribed to the atomic radius of Mn (1.79 Å) being larger than that of Ni (1.62 Å). The unit cell volume of the Gd_2Co_7- and Ce_2Ni_7-type phases as a function of x in $LaY_2Ni_{10.5-x}Mn_x$ (x = 0.0, 0.5, 1.0, 2.0) is shown in Fig. 2. The cell volumes of the Gd_2Co_7- and Ce_2Ni_7-type phases increase linearly with increasing manganese content. The equation for the cell volume of the Gd_2Co_7-type phase in $LaY_2Ni_{10.5-x}Mn_x$ as a function of x is

$$\text{Cell volume } (\text{Å}^3) = 12.59x + 785.54 \quad (1)$$

and the relationship between the cell volume of the Ce_2Ni_7-type phase and x can be expressed as

$$\text{Cell volume } (\text{Å}^3) = 11.47x + 522.56 \quad (2)$$

The strains inside the alloys show a decreasing tendency from 0.18% (x = 0.0) to 0.13% (x = 2.0). There are two main reasons for this: on the one hand, the strain is produced by hydrogen atoms entering the interstitial volume of the alloy lattice [32], which shows that the strain can be released by increasing the cell volume of the Gd_2Co_7- and Ce_2Ni_7-type phases in the alloys with increasing Mn content. On the other hand, the internal strains are assumed to be caused by the mismatch of the constituent subunit parameters of the Gd_2Co_7- and Ce_2Ni_7-type phases, and this mismatch decreases as the abundance difference between the two phases increases [18]. In other words, the greater the abundance difference of the two phases is, the smaller the internal strain of the alloy.

Back-scattered SEM images of the $LaY_2Ni_{10.5-x}Mn_x$ (x = 0.0, 0.5, 1.0, 2.0) alloys are shown in Fig. 3. The alloys exhibit one uniform area in addition to the small number of local black areas in the Mn-free alloy. According to the EDS results (see the inset of x = 0.5, 1.0, 2.0 in Fig. 3), the phase composition of any selected uniform area in the alloys is the same as the nominal composition of the corresponding alloy, which indicates that the Gd_2Co_7-type phase and the Ce_2Ni_7-type phase

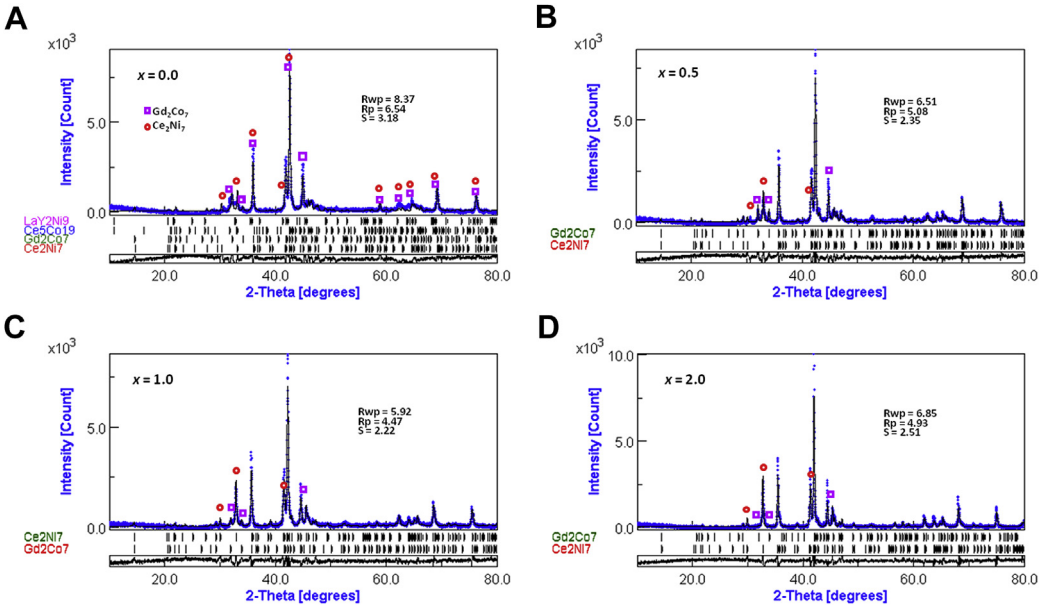

Fig. 1 – Rietveld refinement of the XRD profiles of the $LaY_2Ni_{10.5-x}Mn_x$ (x = 0.0, 0.5, 1.0, 2.0) alloys.

Table 1 – Characteristics of the phases in the $LaY_2Ni_{10.5-x}Mn_x$ ($x = 0.0, 0.5, 1.0, 2.0$) alloys.

Alloy	Phase	Phase abundance (wt %)	Lattice constant			Strain (%)
			a (Å)	c (Å)	v (Å^3)	
$LaY_2Ni_{10.5}$	Gd_2Co_7	51.84 ± 5.1	4.99	36.31	782.64	0.18
	Ce_2Ni_7	44.74 ± 0.3	4.99	24.17	521.42	
	Ce_5Co_{19}	2.04 ± 0.5	4.90	48.97	1019.44	
	$PuNi_3$	1.38 ± 0.3	5.06	24.51	543.18	
$LaY_2Ni_{10}Mn_{0.5}$	Gd_2Co_7	39.48 ± 0.7	5.01	36.46	793.86	0.17
	Ce_2Ni_7	59.88 ± 2.9	5.01	24.31	529.01	
$LaY_2Ni_{9.5}Mn$	Gd_2Co_7	32.68 ± 1.3	5.03	36.57	800.89	0.16
	Ce_2Ni_7	67.31 ± 3.9	5.03	24.39	535.22	
$LaY_2Ni_{8.5}Mn_2$	Gd_2Co_7	23.03 ± 0.5	5.03	36.94	808.83	0.13
	Ce_2Ni_7	76.97 ± 2.3	5.06	24.54	544.71	

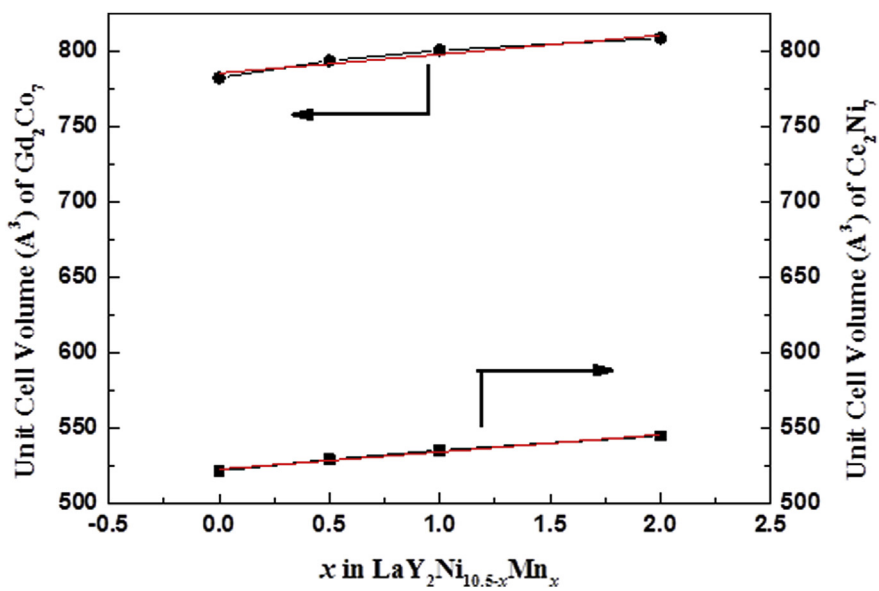

Fig. 2 – Variation of the unit cell volume of the Gd_2Co_7- and Ce_2Ni_7-type phases with x in $LaY_2Ni_{10.5-x}Mn_x$ ($x = 0.0, 0.5, 1.0, 2.0$).

cannot be distinguished from each other in the back-scattered SEM images because they have nearly the same chemical composition [18]. The EDS results indicate that the local black areas in the $x = 0.0$ alloy are of the Ce_5Co_{19}-type phase, which should be the remnant in the corresponding quenched alloy because of incomplete annealing. The inset of $x = 0.0$ in Fig. 3 shows that a greater amount of the Ce_5Co_{19}-type phase exists in the corresponding quenched alloy.

Hydriding/dehydriding properties

Fig. 4 shows the PCI curves of $LaY_2Ni_{10.5-x}Mn_x$ ($x = 0.0, 0.5, 1.0, 2.0$) alloys at 313 K. The plateau pressure of the alloys decreases with increasing Mn content. The plateau pressure can reflect the stability of the hydride phase of a hydrogen storage alloy. The stability of the hydride phase can be correlated with the cell volume in any homologous alloy series [22]. The cell volumes of the Gd_2Co_7- and Ce_2Ni_7-type phases in the $LaY_2Ni_{10.5-x}Mn_x$ ($x = 0.0, 0.5, 1.0, 2.0$) alloys increase with increasing Mn content. Therefore, the stability of the hydride phase in the alloys increases and the plateau pressure of the alloys decreases because the cell volume of the constituent phases increases with increasing Mn content. For alloys containing both the Gd_2Co_7-type phase and the Ce_2Ni_7-type phase, the Gd_2Co_7-type phase with a greater unit cell volume, which can provide more available interstices for H in the lattice, shows a lower hydrogen absorption/desorption plateau pressure [13,15]. Correspondingly, the Ce_2Ni_7-type phase with a smaller unit cell volume shows a higher hydrogen absorption/desorption plateau pressure. One very high pressure plateau (approximately 0.8 MPa for the hydride decomposition pressure) is observed for the $x = 0.0$ alloy. This plateau should be the hydrogen absorption/desorption plateau of the Gd_2Co_7-type phase; predictably, the hydrogen absorption/desorption plateau of the Ce_2Ni_7-type phase is outside the test pressure range (>2 MPa). The $x = 2.0$ alloy shows the lowest pressure plateau (approximately 0.002 MPa) among the alloys. This plateau should be the hydrogen absorption/desorption plateau of the Ce_2Ni_7-type phase; predictably, the hydrogen absorption/desorption plateau of the Gd_2Co_7-type phase is outside the test pressure range ($<10^{-3}$ MPa).

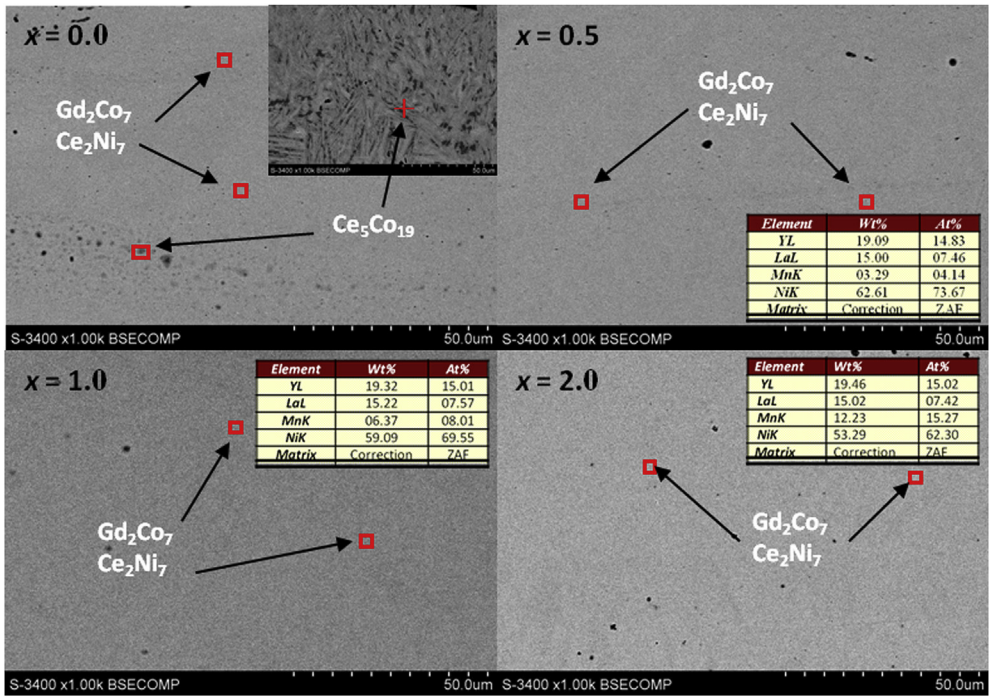

Fig. 3 – SEM images of $LaY_2Ni_{10.5-x}Mn_x$ (x = 0.0, 0.5, 1.0, 2.0) alloys.

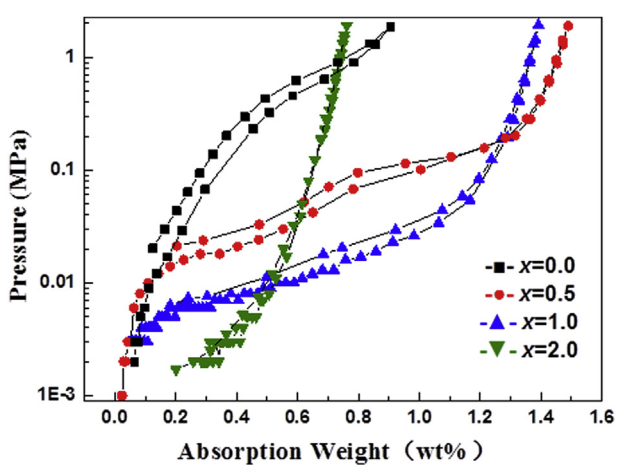

Fig. 4 – Absorption/desorption PCI of $LaY_2Ni_{10.5-x}Mn_x$ (x = 0.0, 0.5, 1.0, 2.0) alloys at 313 K.

Two obvious plateaus are observed for the x = 0.5 alloy. The Gd_2Co_7-type phase shows a lower hydrogen absorption/desorption plateau pressure (approximately 0.02 MPa for the hydride decomposition pressure). Then, there is a higher hydride decomposition pressure for the Ce_2Ni_7-type phase, i.e., approximately 0.1 MPa, which is close to the ambient pressure. The x = 1.0 alloy has two inconspicuous hydrogen absorption/desorption plateaus, which may be correlated with the hydriding reaction mechanism. Typical hydrogen storage alloys show the following phase transition in the hydriding reaction: alloy → solid solution phase (α-phase) → solid solution and hydride coexisting phases (hydrogen absorption plateau) → hydride phase (β-phase). In the dehydriding reaction, the phase transition follows the reverse process of the hydriding reaction. As seen from Fig. 4, the lower the plateau pressure of the alloys is, the less obvious the formation process of the α-phase, which indicates that Mn helps to promote the formation of the β-phase. Thus, the Gd_2Co_7- and Ce_2Ni_7-type phases display close plateau pressures at 313 K for x = 1.0 alloy.

When x increases from 0 to 2, the hydrogen storage capacity first increases from 0.91% (x = 0) to 1.49 wt % (x = 0.5), which is mainly attributed to the decrease in the plateau pressure, which enhances the intrinsic hydrogen storage capacity of the alloys [23–25]. However, when x increases further, the hydrogen storage capacity decreases to 1.39% (x = 1.0) and 0.76 wt % (x = 2.0), which can be attributed to the decrease in the Gd_2Co_7-type phase with a greater unit cell volume. Moreover, the x = 2.0 alloy has the smallest hydrogen storage capacity (only 0.76 wt %) among the alloys, which is also related to its extremely low hydride decomposition pressure.

In summary, an appropriate substitution of Ni by Mn (such as in the x = 0.5 and 1.0 alloys) improves the plateau characteristics and hydrogen storage capacity of the alloys during the hydriding/dehydriding processes. The plateau characteristics include the width, the height, the flatness, and the hysteresis between the hydrogen absorption/desorption plateaus, which reflect the amount of hydrogen storage, the hydrogen absorption/desorption pressures, the hydrogen diffusion velocity, and the reversibility of hydrogen absorption/desorption in turn.

Understanding further the thermodynamic parameters of the hydrogen absorption/desorption reactions of the x = 0.5 alloy with maximum hydrogen storage capacity is necessary. Fig. 5 shows a van't Hoff plot of the logarithmic mid-plateau

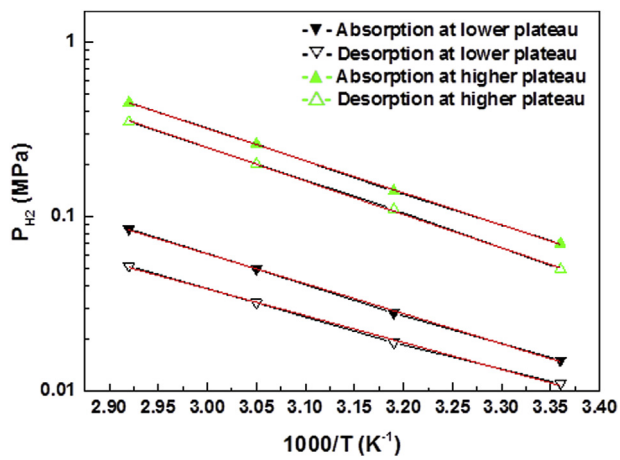

Fig. 5 – Van't Hoff plot of the $LaY_2Ni_{10}Mn_{0.5}$ alloy.

pressure versus the reciprocal of the absolute temperature from the PCI curves of the $LaY_2Ni_{10}Mn_{0.5}$ alloy measured at different temperatures (298 K, 313 K, 328 K, and 343 K). The hydride formation/decomposition enthalpies ΔH, entropies ΔS and Gibbs free energies ΔG of the alloy are calculated as reported in our previous paper [33]. The comprehensive data are summarized in Table 2. The Gibbs free energy ΔG for the absorption of the alloy is negative at room temperature, which indicates that the hydrogenation of the alloy is spontaneous at room temperature. The absolute ΔH values of the hydriding/dehydriding reactions of the two phases in the alloy are in the range of 29.49–36.77 kJ mol^{-1} H_2, which is suitable for the application of the alloy as the active material of the negative electrode in MH–Ni batteries [33].

Furthermore, according to the van't Hoff equation,

$$\ln P_{H2} = \Delta H/RT - \Delta S/R \quad (3)$$

and the formula of the defined Gibbs free energy is

$$\Delta G = \Delta H - T\Delta S \quad (4)$$

The relationship between $\ln P_{H2}$ and ΔG can be represented by the following equations:

$$\ln P_{H2} = \Delta G/RT \quad (5)$$

Eq. (5) shows that the greater the absolute ΔG values of the hydriding reaction of the phase in the alloy are, the lower the hydrogen absorption plateau pressure of the phase at a certain temperature. The Gd_2Co_7 phase has a greater absolute ΔG value for the hydriding reaction than the Ce_2Ni_7 phase, which indicates that the Gd_2Co_7 phase has a lower hydrogen absorption plateau pressure than the Ce_2Ni_7 phase and that the hydrides of the Gd_2Co_7 phase exhibit higher thermodynamic stability. This inference is consistent with the PCI test results.

Discharge and cyclic properties

The discharge potential curves of the $LaY_2Ni_{10.5-x}Mn_x$ (x = 0.0, 0.5, 1.0, 2.0) alloy electrodes are shown in Fig. 6. The electrochemical data of the alloy electrodes are summarized in Table 3. The median discharge voltage of the alloy electrodes is reduced from 1.297 V (x = 0.0) to 1.248 V (x = 2.0), which indicates that the partial substitution of Mn for Ni leads to increases in the discharge overpotential of the alloy electrode to different extents [20]. According to the Nernst Eq. (6), the variation trend of the equilibrium potential (E_{eq}) in the discharge potential curves is consistent with that of the hydrogen equilibrium pressure (P_{eq}) in the PCI curves [18].

$$E_{eq}\ (\text{versus Hg/HgO}) = -0.925 - 0.03 \log (P_{eq}) \quad (6)$$

Moreover, Mn ions that dissolve from the negative electrode alloy deposit onto the separator [34], which also increases the discharge overpotential of the alloy electrode due to the increase in the polarization resistance in the experimental cell [16].

The voltage plateau of the x = 0.0 alloy, whose discharge capacity is only 207.5 mAh g^{-1}, is narrow. By contrast, the addition of Mn widens and smooths the discharge voltage plateaus and markedly increases the discharge capacity of the alloy electrodes. Specifically, the discharge capacity increases to 392.9 mAh g^{-1} (x = 0.5) and 389.3 mAh g^{-1} (x = 1.0), which is significantly higher than that reported in the literatures on the study of the enhanced discharge capacity in A_2B_7 based alloy electrodes [24,26]. Moreover, the discharge capacity of the x = 2.0 alloy electrode is 366.6 mAh g^{-1}, which is significantly higher than that of the x = 0.0 alloy electrode. Thus, the partial substitution of Ni by Mn in the $LaY_2Ni_{10.5}$ alloy can significantly improve the alloy's voltage plateau characteristics and increase its discharge capacity. As expected, the evolution of the electrode discharge capacity essentially follows the same trend as the hydrogen storage capacity [18,22], as indicated by the PCI curves (see Section Hydriding/dehydriding properties of this paper). However, the hydrogen storage capacity (0.76 wt %) of the x = 2.0 alloy is smaller than that (0.91 wt %) of the x = 0.0 alloy in the solid–H_2 reaction, while its discharge capacity (366.6 mAh g^{-1}) is much greater than that (207.5 mAh g^{-1}) of the x = 0.0 alloy in the electrochemical reaction. This phenomenon is related to their different plateau pressure values, as shown in the PCI curves. The plateau pressure of the x = 0.0 alloy is much higher than the ambient pressure, which causes a large amount of hydrogen to escape during the charging/discharging processes and leads to a low

Table 2 – Thermodynamic parameters of the $LaY_2Ni_{10}Mn_{0.5}$ alloy.

Alloy	Phases	ΔH/kJ·mol^{-1} H_2		ΔS/J·K^{-1} mol^{-1} H_2		ΔG/kJ·mol^{-1} H_2(298 K)	
		Absorption	Desorption	Absorption	Desorption	Absorption	Desorption
x = 0.5	Gd_2Co_7	−32.94 (±0.67)	29.49 (±0.80)	−75.45 (±2.11)	61.28 (±2.49)	−10.46 (±0.04)	11.23 (±0.06)
	Ce_2Ni_7	−35.24 (±0.40)	36.77 (±0.54)	−96.32 (±1.25)	98.62 (±1.68)	−6.54 (±0.03)	7.38 (±0.04)

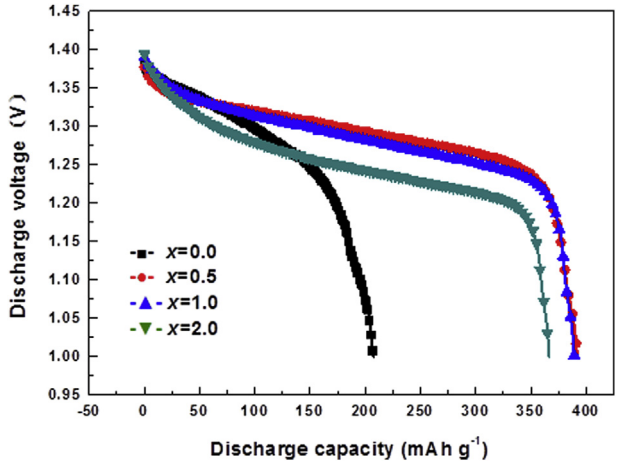

Fig. 6 – Discharge potential curves of $LaY_2Ni_{10.5-x}Mn_x$ ($x = 0.0, 0.5, 1.0, 2.0$) alloy electrodes (298 K).

utilization efficiency of the hydrogen. The largest amount of hydrogen stored in the $x = 2.0$ alloy with a very low plateau pressure during the charging processes can participate in the electrochemical reaction by the action of electrical energy during the discharging processes. Similarly, the hydrogen storage capacity (1.49 wt %) of the $x = 0.5$ alloy is much greater than that (1.39 wt %) of the $x = 1.0$ alloy in the solid–H_2 reaction, while their discharge capacities (392.9 mAh g^{-1} for $x = 0.5$ alloy, 389.3 mAh g^{-1} for $x = 1.0$ alloy) are almost the same in the electrochemical reaction.

The relationship between the discharge capacity and the number of cycles of the $LaY_2Ni_{10.5-x}Mn_x$ ($x = 0.0, 0.5, 1.0, 2.0$) alloy electrodes is shown in Fig. 7. From Fig. 7(a) (1–10 cycles) and Table 3, it can be seen that the $x = 0.0$, 0.5, and 1.0 alloy electrodes can be easily activated to reach their maximum capacity within two cycles. However, the discharge capacity of the $x = 2.0$ alloy electrode is close to the maximum discharge capacity within four cycles, which shows that its activation capability is the worst among the alloys. The changing trend of the activation capability with Mn content is different from that reported in the literature on the study of the effect of the Mn content on the electrochemical characteristics of A_2B_7- and AB_5-type La–(Ce)–Mg–Ni–Mn–Co alloys [22,24,25], which may be attributed to the different alloy systems and different compositions. In general, the hydrogen storage electrode alloy with a multiphase structure has good activation performance

Table 3 – Electrochemical properties of $LaY_2Ni_{10.5-x}Mn_x$ ($x = 0.0, 0.5, 1.0, 2.0$) alloy electrodes.

Alloys	N^a	$U_m{}^b$ (V)	$C_{max}{}^c$ (mAh g^{-1})	$S_{400}{}^d$ (%)
$x = 0.0$	1	1.297	207.5	69.9
$x = 0.5$	2	1.294	392.9	56.3
$x = 1.0$	2	1.283	389.3	60.2
$x = 2.0$	4	1.248	366.6	58.5

[a] N is the number of cycles required to activate the electrodes.
[b] U_m is the median discharge voltage of the half-cell consisting of the alloy electrodes.
[c] C_{max} is the maximum discharge capacity of the alloy electrodes.
[d] S_{400} is the capacity retention ratio after 400 cycles.

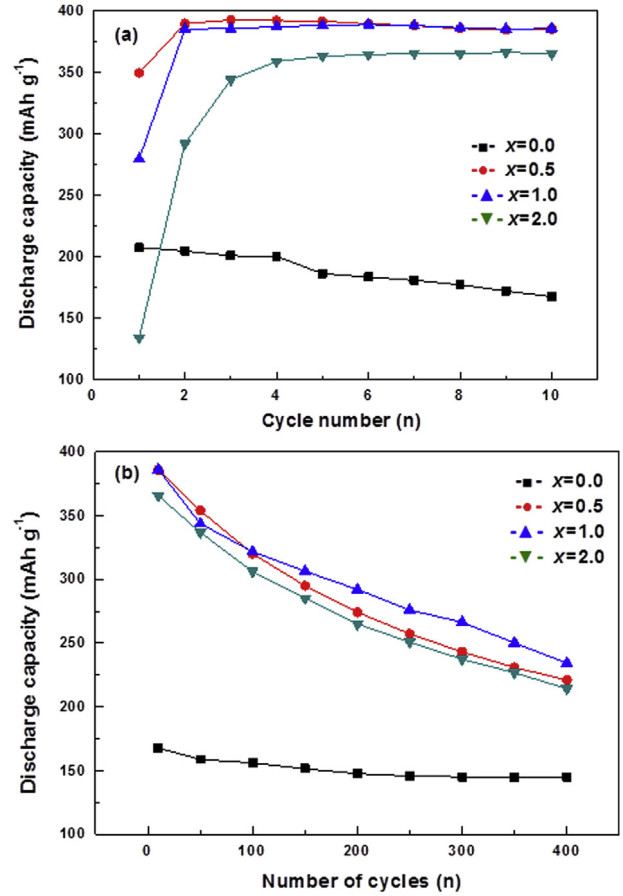

Fig. 7 – Discharge capacity versus number of cycles for $LaY_2Ni_{10.5-x}Mn_x$ ($x = 0.0, 0.5, 1.0, 2.0$) alloy electrodes: (a) 0–10 cycles; (b) 10–400 cycles.

because the phase boundary can decrease the lattice distortion and strain energy formed in the process of charging and provide good tunnels for the diffusion of hydrogen atoms, thus improving the activation performance of the alloys [32,35]. Nevertheless, it is well known that the electrocatalytic effect of Mn is far less than that of Ni for the charging/discharging reaction of the hydrogen storage alloy electrode, and thus, the high content of Mn will decrease the activation performance of the alloy electrode.

Table 3 lists the capacity retention ratios of the alloy electrodes after the 400th cycle (S_{400}). The capacity retention ratio is the ratio of the discharge capacity to the maximum discharge capacity during the cycle test, and it represents the cyclic stability of the alloy electrodes [36]. From Fig. 7(b) (10–400 cycles) and Table 3, it can be seen that the capacity retention ratio of the $x = 0.0$ alloy is 69.9%, and the capacity retention ratios of the Mn-containing alloys are 56.3% ($x = 0.5$), 60.2% ($x = 1.0$), and 58.5% ($x = 2.0$). The cyclic stability of the $LaY_2Ni_{10.5-x}Mn_x$ ($x = 0.0, 0.5, 1.0, 2.0$) alloy electrodes is rather good, in spite of the cyclic stability of the Mn-containing alloy electrodes being lower. It has been reported that the discharge capacity degradation of Mn-containing rare-earth-based hydrogen storage alloy electrodes is mainly caused by the dissolution of Mn [23]. For AB_3- and A_2B_7-type La–(Ce)–Mg–Ni–Mn–Co alloys, the cyclic stability of the alloy electrodes

gradually decreases with increasing Mn content, although the inclusion of Co would effectively prevent the corrosion of Mn in the system alloys [22–24]. However, the Mn content has no serious negative effect on the electrochemical cyclic stability of the Co-free La–Y–Ni alloys in the present study. From Table 1, it can be seen that the internal strain of the alloys decreases with increasing substitution of Mn for Ni. In general, the strain arising from the lattice expansion and contraction can induce pulverization of the alloy during the hydrogenation/dehydrogenation process. As a result, the fresh alloy surface is exposed directly to the alkaline electrolyte, and then, the active components are easily oxidized, which leads to the capacity degradation of the alloy electrodes [37]. Thus, a decrease in the strain of the alloys is favorable for improving the anti-pulverization capability of the alloy particles [14] and reduces the adverse effects of Mn on the cyclic stability.

Electrochemical kinetic properties

The high-rate dischargeability (HRD), which is defined and calculated as reported in a previous paper [38], reflects the electrochemical kinetics of alloy electrodes. Fig. 8 shows the relationship between the HRD and the discharge current density of the $LaY_2Ni_{10.5-x}Mn_x$ (x = 0.0, 0.5, 1.0, 2.0) alloy electrodes. In this study, the discharge current density I_d is 300, 900, and 1500 mA g^{-1}. The characteristics of the reaction kinetics are summarized in Table 4. From Fig. 8, it can be seen that the variation trend of HRD at I_d = 300 mA g^{-1} is in line with the discharge capacity order at a low current density (0.2 C rate). The HRD first increases and then decreases with increasing x at high discharge current densities (900 and 1500 mA g^{-1}). From Table 4, it can be seen that HRD_{1500} first increases from 43% (x = 0.0) to 50% (x = 0.5) and then decreases to 15% (x = 1.0) and 14% (x = 2.0). This variation is consistent with the results obtained from the study on the effect of the Mn content on the HRD of AB_3-, A_2B_7- and AB_5-type La–(Ce)–Mg–Ni–Mn–Co alloys [22–25].

The discharge process of hydrogen storage alloy electrodes is mainly divided into two steps: charge transfer on the alloy electrode surface and hydrogen diffusion in the bulk alloy.

Table 4 – Characteristics of reaction kinetics of $LaY_2Ni_{10.5-x}Mn_x$ (x = 0.0, 0.5, 1.0, 2.0) alloy electrodes.

Alloys	I_0 (mA·g^{-1})	D (×10^{-10} cm^2 s^{-1})	HRD_{900} [a] (%)	HRD_{1500} [a] (%)
x = 0.0	73.76 (±2.00)	1.71 (±0.02)	51	43
x = 0.5	104.86 (±0.64)	4.36 (±0.01)	54	50
x = 1.0	116.16 (±0.93)	1.30 (±0.01)	40	15
x = 2.0	139.04 (±1.44)	1.20 (±0.01)	21	14

[a] HRD_{900} and HRD_{1500} are the high-rate dischargeabilities at discharge current densities I_d = 900 mA g^{-1} and I_d = 1500 mA g^{-1}, respectively.

The synergy between these steps determines the HRD of alloy electrodes [19,38]. In other words, the HRD is jointly influenced by the exchange current density I_0, which reflects the electrocatalytic activity of the charge transfer reaction on the alloy electrode surface, and the hydrogen diffusion coefficient D, which reflects the hydrogen diffusion ability in the bulk alloy.

Fig. 9 shows the linear polarization curves of the $LaY_2Ni_{10.5-x}Mn_x$ (x = 0.0, 0.5, 1.0, 2.0) alloy electrodes at 50% DOD and room temperature (298 K). The polarization current density linearly depends on the potential in such a small overpotential range. Then, the exchange current density I_0 can be calculated from the slopes (I_d/η) of the polarization curves [39].

$$I_0 = I_d RT/F\eta \quad (7)$$

where R is the gas constant, T is the absolute temperature, F is the Faraday constant, η is the total overpotential, and I_d is the applied current density. From Table 4, it can be seen that the exchange current density I_0 of the alloy electrodes increases from 75.30 mA g^{-1} (x = 0.0) to 140.32 mA g^{-1} (x = 2.0) with increasing Mn content. For rare-earth-based hydrogen storage electrode alloys, the partial substitution of Mn for Ni can increase the Ni content at the alloy surface due to the oxidation and dissolution of Mn, which is mainly ascribed to the electrode potential of Mn (−1.56 V) being more negative than that of Ni (−0.72 V) in alkaline solution, and thus increase the active surface area of the Mn-substituted alloy electrode, which leads to good electrocatalytic properties to improve the

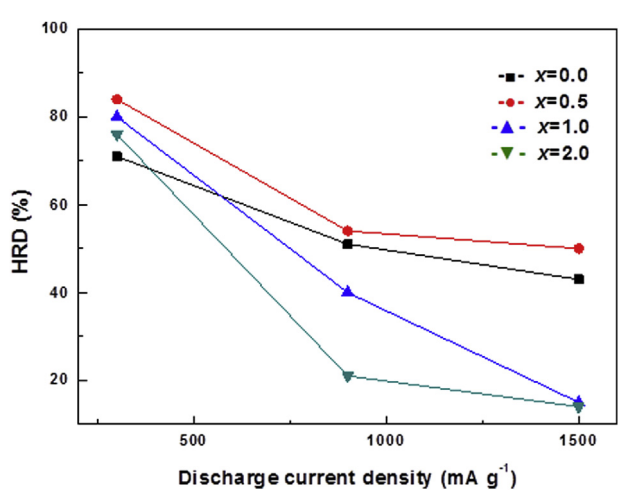

Fig. 8 – HRD of $LaY_2Ni_{10.5-x}Mn_x$ (x = 0.0, 0.5, 1.0, 2.0) alloy electrodes at 298 K.

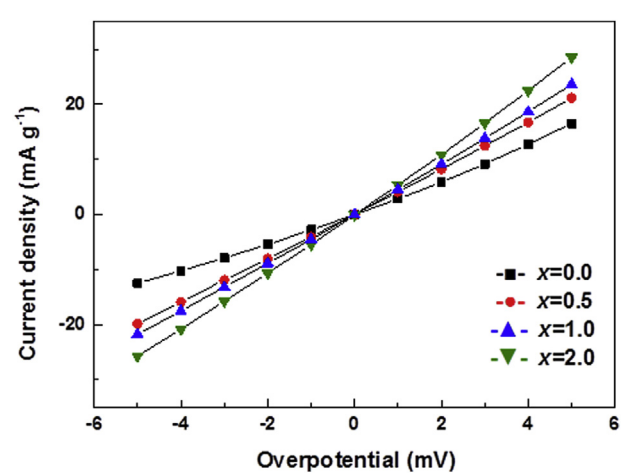

Fig. 9 – Linear polarization curves of $LaY_2Ni_{10.5-x}Mn_x$ (x = 0.0, 0.5, 1.0, 2.0) alloy electrodes at 50% DOD.

reaction rate of hydrogen [20,23,25]. From the change trend of the I_0 value, the HRD should increase with increasing Mn content. In fact, the HRDs of the $x > 0.5$ alloys decrease with increasing Mn content, which shows that the hydrogen diffusion coefficient D is an important factor that can influence the HRD.

Fig. 10 shows semilogarithmic curves of the anodic current versus the response time of the $LaY_2Ni_{10.5-x}Mn_x$ ($x = 0.0$, 0.5, 1.0, 2.0) alloy electrodes at room temperature (298 K). The hydrogen diffusion coefficient D can be calculated from the linear portion of the corresponding curves by Ref. [40].

$$\log i = \log (6FD(C_0-C_s)/da^2) - (\pi^2/2.303)\,(D/a^2)t \quad (8)$$

where i, D, d, a, C_0, C_s, and t are the diffusion current density (A g^{-1}), diffusion coefficient of hydrogen ($cm^2\ s^{-1}$), density of the hydrogen storage alloy (g cm^3), alloy particle radius (22.35×10^{-4} cm in this study), initial hydrogen concentration in the bulk alloy (mol cm^3), hydrogen concentration on the surface of the alloy particles (mol cm^3), and discharge time (s), respectively.

From Table 4, it can be seen that the diffusion coefficient of hydrogen first increases from 1.71×10^{-10} $cm^2\ s^{-1}$ ($x = 0.0$) to 4.36×10^{-10} $cm^2\ s^{-1}$ ($x = 0.5$) and then decreases to 1.30×10^{-10} $cm^2\ s^{-1}$ ($x = 1.0$) and 1.20×10^{-10} $cm^2\ s^{-1}$ ($x = 2.0$), which is consistent with the variation of the HRD of the alloy electrodes. Thus, the hydrogen diffusion coefficient is the rate-determining factor in the electrochemical reaction at high discharge current densities. The variation tendency of the hydrogen diffusion coefficient is related to the number of phase boundaries in the alloys. The boundaries can provide channels for hydrogen diffusion [41,42]. The greater the number of boundaries is, the greater the diffusion coefficient. The number of phase boundaries is related to both the phase quantity and the phase abundance difference in the alloys. A greater phase quantity and smaller phase abundance difference can generate a greater number of phase boundaries [43]. Therefore, the $x = 0.0$ alloy should have good hydrogen diffusion ability. However, the D value of the $x = 0.5$ alloy is the largest among these alloys, which could be attributed to the initial hydrogen concentration in the bulk alloy. Eq. (8) shows that the difference (C_0–C_s) between the initial hydrogen concentration (C_0) in the bulk alloy and hydrogen concentration (C_s) on the surface of the alloy particles is an important factor affecting D value. The difference (C_0–C_s) is the driving force of hydrogen diffusion. The greater the driving force is, the greater the diffusion coefficient. Normally, the C_s values between different alloys should be similar. Thus, the great C_0 value of the $x = 0.5$ alloy is bound to result in an improving hydrogen diffusion ability.

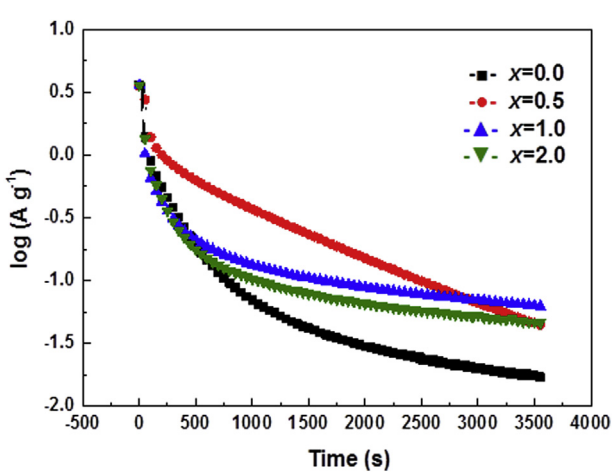

Fig. 10 – Semilogarithmic curves of anodic current versus response time of $LaY_2Ni_{10.5-x}Mn_x$ ($x = 0.0$, 0.5, 1.0, 2.0) alloy electrodes.

Conclusions

(1) The A_2B_7-type La–Y–Ni–Mn alloys investigated in our study constitute a system of new hydrogen storage materials. $LaY_2Ni_{10.5-x}Mn_x$ ($x = 0.0$, 0.5, 1.0, 2.0) alloys consist of Gd_2Co_7- and Ce_2Ni_7-type phases. With the addition of Mn, the abundance of the Ce_2Ni_7-type phase increases from 44.74% ($x = 0.0$) to 76.97% ($x = 2.0$). The lattice parameters and cell volumes of both the Gd_2Co_7- and Ce_2Ni_7-type phases increase with increasing x. The internal strains show a decreasing tendency with increasing x.

(2) The PCI curves reveal that the hydrogen storage capacity increases first and then decreases upon increasing x from 0.0 to 2.0, and the equilibrium pressure decreases.

(3) The electrochemical measurements show that the maximum discharge capacity (392.9 mAh g^{-1}) of the $LaY_2Ni_{10}Mn_{0.5}$ alloy markedly exceeds that (372 mAh g^{-1}) of the commercial $LaNi_5$ alloy. The capacity retention ratios of the alloy electrodes are as high as 69.9% ($x = 0.0$), 56.3% ($x = 0.5$), 60.2% ($x = 1.0$), and 58.5% ($x = 2.0$) after the 400th cycle. For a discharge current density of 1500 mA g^{-1}, the high-rate dischargeability of the alloy electrodes first increases from 43% ($x = 0$) to 50% ($x = 0.5$) and then decreases to 14% ($x = 2.0$). Linear polarization and potential step measurements show that the exchange current density I_0 of the alloy electrodes increases and the hydrogen diffusion coefficient D of the alloy electrodes first increases and then decreases with increasing Mn content, which suggests that the hydrogen diffusion coefficient is the rate-determining factor of the electrochemical reaction at high discharge current densities.

To summarize, it is confirmed that in the $LaY_2Ni_{10.5-x}Mn_x$ ($x = 0.0$, 0.5, 1.0, 2.0) hydrogen storage alloys, there is an optimum Mn substitution ($x = 0.5$) for Ni in terms of the thermodynamic and kinetic properties and the solid–H_2 and electrochemical reaction characteristics.

Acknowledgments

This work was supported by the Key International Science and Technology Cooperation Projects of the Ministry of Science and Technology of the PRC (2010DFB63510, 2013DFR50940) and the National Nature Science Foundation of China (51061001).

REFERENCES

[1] Latroche M, Baddour-Hadjean R, Percheron-Guégan A. Crystallographic and hydriding properties of the system $La_{1-x}Ce_xY_2Ni_9$ (x_{Ce} = 0, 0.5 and 1). J Solid State Chem 2003;173:236–43.

[2] Hu WK, Zhang YS, Song DY, Shen PW. Electrochemical hydrogen storage property of amorphous and crystalline Ml-Ni alloy films. Int J Hydrogen Energy 1996;21:651–6.

[3] Anik M, Aybar AB, Küçükdeveci N, Erken H, Baksan B, Gaşan H, et al. Synthesis of La_2Ni_7 hydrogen storage alloy by the electro-deoxidation technique. Int J Hydrogen Energy 2015;40:2248–54.

[4] Zhang DY, Tang JK, Gschneidner Jr KA. A redetermination of the La-Ni phase diagram from LaNi to $LaNi_5$ (50-83.3 at%Ni). J Less-Common Met 1991;169:45–53.

[5] Zhang XB, Yin WY, Chai YJ, Zhao MS. Structure and electrochemical characteristics of $RENi_3$ alloy. Mater Sci Eng B 2005;117:123–8.

[6] Baddour-Hadjean R, Meyer L, Pereira-Ramos JP, Latroche M, Percheron-Guégan A. An electrochemical study of new $La_{1-x}Ce_xY_2Ni_9$ ($0 \le x \le 1$) hydrogen storage alloys. Electrochim Acta 2001;46:2385–93.

[7] Baddour-Hadjean R, Pereira-Ramos JP, Latroche M, Percheron-Guegan A. New ternary intermetallic compounds belonging to the R-Y-Ni (R = La, Ce) system as negative electrodes for Ni-MH batteries. J Alloy Compd 2002;330–332:782–6.

[8] Zhang J, Fang F, Zheng SY, Zhu J, Chen GR, Sun DL, et al. Hydrogen-induced phase transitions in RNi_3 and RY_2Ni_9 (R = La, Ce) compounds. J Power Sources 2007;172:446–50.

[9] Kohno T, Yoshida H, Kawashima F, Inaba T, Sakai I, Yamamoto M, et al. Hydrogen storage properties of new ternary system alloys: La_2MgNi_9, $La_5Mg_2Ni_{23}$, La_3MgNi_{14}. J Alloy Compd 2000;311:L5–7.

[10] Young K, Ouchi T, Shen H, Bendersky LA. Hydrogen induced amorphization of $LaMgNi_4$ phase in metal hydride alloys. Int J Hydrogen Energy 2015;40:8941–7.

[11] Li YM, Ren HP, Zhang YH, Liu ZC, Zhang HW. Hydrogen induced amorphization behaviors of multiphase $La_{0.8}Mg_{0.2}Ni_{3.5}$ alloy. Int J Hydrogen Energy 2015;40:7093–102.

[12] Yan HZ, Xiong W, Wang L, Li BQ, Li J, Zhao X. Investigations on AB_3-, A_2B_7- and A_5B_{19}-type La-Y-Ni system hydrogen storage alloys. Int J Hydrogen Energy 2016. http://dx.doi.org/10.1016/j.ijhydene.2016.09.049.

[13] Ma ZW, Zhu D, Wu CL, Zhong CL, Wang QN, Zhou WH, et al. Effects of Mg on the structures and cycling properties of the $LaNi_{3.8}$ hydrogen storage alloy for negative electrode in Ni/MH battery. J Alloy Compd 2015;620:149–55.

[14] Zhang JX, Villeroy B, Knosp B, Bernard P, Latroche M. Structural and chemical analyses of the new ternary La_5MgNi_{24} phase synthesized by spark plasma sintering and used as negative electrode material for Ni-MH batteries. Int J Hydrogen Energy 2012;37:5225–33.

[15] Liao B, Lei YQ, Chen LX, Lu GL, Pan HG, Wang QD. Effect of the La/Mg ratio on the structure and electrochemical properties of $La_xMg_{3-x}Ni_9$ (x = 1.6-2.2) hydrogen storage electrode alloys for nickel-metal hydride batteries. J Power Sources 2004;129:358–67.

[16] Dong XP, Lü FX, Zhang YH, Yang LY, Wang XL. Effect of La/Mg on the structure and electrochemical performance of La-Mg-Ni system hydrogen storage electrode alloy. Mater Chem Phys 2008;108:251–6.

[17] Liu JJ, Han SM, Li YJ, Zhang L, Zhao YM, Che LD. Effect of crystal transformation on electrochemical characteristics of La-Mg-Ni-based alloys with A_2B_7-type super-stacking structures. Int J Hydrogen Energy 2013;38:14903–11.

[18] Liu JJ, Han SM, Han D, Li Y, Yang SQ, Zhang L, et al. Enhanced cycling stability and high rate dischargeability of $(La,Mg)_2Ni_7$-type hydrogen storage alloys with $(La,Mg)_5Ni_{19}$ minor phase. J Power Sources 2015;287:237–46.

[19] Ouyang LZ, Cao ZJ, Li LL, Wang H, Liu JW, Min D, et al. Enhanced high-rate discharge properties of $La_{11.3}Mg_{6.0}Sm_{7.4}Ni_{61.0}Co_{7.2}Al_{7.1}$ with added graphene synthesized by plasma milling. Int J Hydrogen Energy 2014;39:12765–72.

[20] Liao B, Lei YQ, Chen LX, Lu GL, Pan HG, Wang QD. A study on the structure and electrochemical properties of $La_2Mg(Ni_{0.95}M_{0.05})_9$ (M = Co, Mn, Fe, Al, Cu, Sn) hydrogen storage electrode alloys. J Alloy Compd 2004;376:186–95.

[21] Liu JJ, Han SM, Li Y, Zhao X, Yang SQ, Zhao YM. Cooperative effects of Sm and Mg on electrochemical performance of La-Mg-Ni-based alloys with A_2B_7- and A_5B_{19}-type super-stacking structure. Int J Hydrogen Energy 2015;40:1116–27.

[22] Pan HG, Jin QW, Gao MG, Liu YF, Li R, Lei YQ, et al. An electrochemical study of $La_{0.4}Ce_{0.3}Mg_{0.3}Ni_{2.975-x}Mn_xCo_{0.525}$ (x = 0.1-0.4) hydrogen storage alloys. J Alloy Compd 2004;376:196–204.

[23] Liu YF, Pan HG, Gao MX, Zhu YF, Lei YQ, Wang QD. The effect of Mn substitution for Ni on the structural and electrochemical properties of $La_{0.7}Mg_{0.3}Ni_{2.55-x}Co_{0.45}Mn_x$ hydrogen storage electrode alloys. Int J Hydrogen Energy 2004;29:297–305.

[24] Zhang XB, Sun DZ, Yin WY, Chai YJ, Zhao MS. Effect of Mn content on the structure and electrochemical characteristics of $La_{0.7}Mg_{0.3}Ni_{2.975-x}Co_{0.525}Mn_x$ (x = 0-0.4) hydrogen storage alloys. Electrochim Acta 2005;50:2911–8.

[25] Liu YF, Pan HG, Zhu YF, Li R, Lei YQ. Influence of Mn content on the structural and electrochemical properties of the $La_{0.7}Mg_{0.3}Ni_{4.25-x}Co_{0.75}Mn_x$ hydrogen storage alloys. Mater Sci Eng A 2004;372:163–72.

[26] Cao ZJ, Ouyang LZ, Li LL, Lu YS, Wang H, Liu JW, et al. Enhanced discharge capacity and cycling properties in high-samarium, praseodymium/neodymium-free, and low-cobalt A_2B_7 electrode materials for nickel-metal hydride battery. Int J Hydrogen Energy 2015;40:451–5.

[27] Yan HZ, Xiong W, Wang L, Li BQ, Li J. A kind of yttrium-nickel-rare earth system hydrogen storage alloy. Chinese patent CN201410429187.7. 2014.

[28] Yan HZ, Li BQ, Xiong W, Wang L, Li J. A kind of yttrium-nickel-rare earth system hydrogen storage alloy. Chinese patent CN201410429202.8. 2014.

[29] Yan HZ, Li BQ, Xiong W, Wang L, Li J. A kind of yttrium-nickel-rare earth system hydrogen storage alloy and secondary battery containing the hydrogen storage alloy. Chinese patent CN201410427281.9. 2014.

[30] Young K, Wong DF, Wang L, Nei J, Ouchi T, Yasuoka S. Mn in misch-metal based superlattice metal hydride alloy – Part 1 structural, hydrogen storage and electrochemical properties. J Power Sources 2015;277:426–32.

[31] Ouyang LZ, Cao ZJ, Wang H, Liu JW, Sun DL, Zhang QA, et al. Dual-tuning effect of in on the thermodynamic and kinetic properties of Mg_2Ni dehydrogenation. Int J Hydrogen Energy 2013;38:8881–7.

[32] Zhang YH, Li BW, Ren HP, Cai Y, Dong XP, Wang XL. Effects of Cr addition on the microstructures and electrochemical properties of as-cast and quenched $La_2Mg(Ni_{0.85}Co_{0.15})_9$ electrode alloys. J Alloy Compd 2007;436:209–15.

[33] Xiong W, Li BQ, Wang L, Li J, Kong FQ, Yan HZ. Investigation of the thermodynamic and kinetic properties of La-Fe-B system hydrogen-storage alloys. Int J Hydrogen Energy 2014;39:3805–9.

[34] Teraoka H. Development of low self-discharge nickel-metal hydride battery, Available online: http://www.scribd.com/doc/9704685/Teraoka-Article-En [Accessed 30 September 2015].

[35] Li M, Han SM, Li Y, Guan W, Mao LR, Hu L. Study on the phase structure and electrochemical properties of $RE_{0.93}Mg_{0.07}Ni_{2.96}Co_{0.60}Mn_{0.37}Al_{0.17}$ hydrogen storage alloy. Electrochim Acta 2006;51:5926–31.
[36] Wang L, Yan HZ, Xiong W, Li BQ, Li J, Kong FQ. The influence of boron content on the structural and electrochemical properties of the $La_{15}Fe_{77}B_8$-type hydrogen storage alloy. J Power Sources 2014;259:213–8.
[37] Liu YF, Pan HG, Yue YJ, Zhu YF, Wu XF, Chen N, et al. Cycling durability and degradation behavior of La-Mg-Ni-Co-type metal hydride electrodes. J Alloy Compd 2005;395:291–9.
[38] Yan HZ, Kong FQ, Xiong W, Li BQ, Li J, Wang L. New La-Fe-B ternary system hydrogen storage alloys. Int J Hydrogen Energy 2010;35:5687–92.
[39] Popov BN, Zheng G, White RE. Determination of transported and electrochemical kinetic parameters of M-H electrodes. J Appl Electrochem 1996;26:603–11.
[40] Moussa MB, Abdellaoui M, Mathlouthi H, Lamloumi J, Guégan AP. Investigation of the cycle stability and diffusivity of hydrogen in the $MmNi_{3.55}Mn_{0.4}Al_{0.3}Co_{0.6}Fe_{0.15}$ compound. J Alloy Compd 2006;407:256–62.
[41] Li RF, Wan J, Wang F, Ding CP, Yu RH. Effect of non-stoichiometry on microstructure and electrochemical performance of $La_{0.8}Gd_xMg_{0.2}Ni_{3.15}Co_{0.25}Al_{0.1}$ ($x = 0$-0.4) hydrogen storage alloys. J Power Sources 2016;301:229–36.
[42] Tian X, Yun GH, Wang HY, Shang T, Yao ZQ, Wei W, et al. Preparation and electrochemical properties of La-Mg-Ni-based $La_{0.75}Mg_{0.25}Ni_{3.3}Co_{0.5}$ multiphase hydrogen storage alloy as negative material of Ni/MH battery. Int J Hydrogen Energy 2014;39:8474–81.
[43] Zhang JL, Han SM, Li Y, Liu JJ, Yang SQ, Zhang L, et al. Effects of $PuNi_3$- and Ce_2Ni_7-type phase abundance on electrochemical characteristics of La-Mg-Ni-based alloys. J Alloy Compd 2013;581:693–8.